Article:
Ward, JA and Wilson, RE (2011) Criteria for convective versus absolute string instability in car-following models. Proceedings of the Royal Society of London: Mathematical, Physical and Engineering Sciences, 467 (2132). pp. 2185-2208. ISSN 1364-5021

https://doi.org/10.1098/rspa.2010.0437

Criteria for convective versus absolute string instability in car-following models

By Jonathan A. Ward[1,†] and R. Eddie Wilson[2]

[1]*MACSI, Department of Mathematics and Statistics, College of Science and Engineering, University of Limerick, Limerick, Republic of Ireland*
[2]*Department of Engineering Mathematics, University of Bristol, Queen's Building, University Walk, Bristol BS8 1TR, UK*

The linear stability properties of car-following models of highway traffic are analysed. A general family of models is introduced and the subsequent analysis developed in terms of its partial derivatives. Two measures of wave propagation, namely (i) the group velocity and (ii) the signal velocity, are introduced and computed. These measures are used to classify how instability propagates disturbances, measured relative to the frame of the road along which the vehicles drive. Detector data suggest that disturbances should propagate only in an upstream direction (convective upstream instability) and it is shown how to parametrise models to agree with data and avoid unrealistic downstream propagation (absolute and convective downstream instability).

Keywords: highway traffic; car-following models; instability; wave propagation

1. Introduction

Since the mid-1990s, there has been an intense and sometimes argumentative discussion about the spatio-temporal patterns observed in highway traffic flow, see for example Kerner & Rehborn (1996, 1997); Kerner (2002*a*,*b*); Treiber *et al.* (2000); Helbing *et al.* (2009); Schönhof & Helbing (2009); Treiber *et al.* (2010). A typical spatio-temporal pattern is displayed in figure 1. The features of interest are a region of congestion developing at an on-ramp, out of which nucleate *stop-and-go* waves, which propagate upstream at about 15 to 20km/h — a figure that seems almost universal in that it has been observed on highways in many different countries across the Western world (Zielke *et al.*, 2008). One explanation for stop-and-go waves is that uniform traffic flow is unstable (either linearly or non-linearly) under certain conditions. The inevitable fluctuations (due to lane-changing, noise etc.) at the level of individual vehicles then become magnified so as to result in large amplitude patterns with macroscopic spatial scales (i.e., much longer than the range of the individual vehicle interactions).

To understand the 'up-scaling' process, we analyse the stability properties of car-following models that describe vehicles as discrete entities moving in continuous space and time, whose motions solve simple ordinary (or delay) differential equations coupling the motion of nearest neighbours. In terms of the linear stability properties that we focus on here, this analysis began in the late 1950s (Chandler

† Author for correspondence (jonathan.ward@ul.ie)

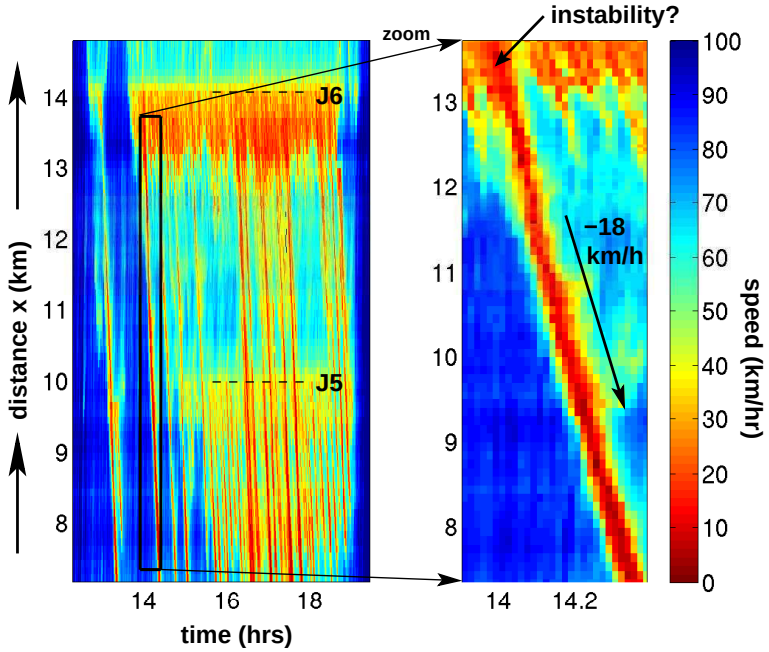

Figure 1. An example of spatio-temporal patterns in inductance loop data from the north-bound M42 Motorway in the UK. This kind of spatially extended pattern is a common feature of highways around the world (Treiber *et al.*, 2010). Distance in kilometres is plotted on the vertical axis against time in hours on the horizontal axis. Colour corresponds to speed in kilometres per hour. There are two junctions present in this figure, labelled J5 and J6. Drivers travel up the page, in the direction of increasing distance and time. A zone of congestion (sometimes called *synchronized flow*) builds at J6, due to the combined volume of the main carriageway and on-ramp flow. The region of *synchronized flow* has a stationary downstream front which remains fixed at the junction. However, numerous stop-and-go waves emerge in an upstream direction, propagating against the flow of the traffic.

et al., 1958). In particular, Herman *et al.* (1959) developed the concept now known as *string* instability, in which a growing wave envelope may propagate up a column of vehicles, even when the 'local' dynamics of each individual vehicle are stable. In mathematical language, *string* instability is a special case of *convective* spatio-temporal instability, in that growth is via a localised travelling envelope, in contrast to *absolute* instability where the linearised model experiences blow-up at all points in the spatial domain.

In realistic traffic models, driver behaviour is governed by vehicles in front, rather than behind, so instability is necessarily convective when measured in the frame of the vehicles. The complication is that data such as figure 1 are presented in the frame of the road, rather than in the frame of the vehicles, each of which is driving forward relative to the road. So an instability which is convective in the vehicle frame can be either absolute or convective in the road frame, depending on whether vehicles drive forward faster than the wave envelope propagates backwards relative to them. See figure 2. The importance of this distinction between convective and absolute instability in the vehicle and road frames has been recognised by

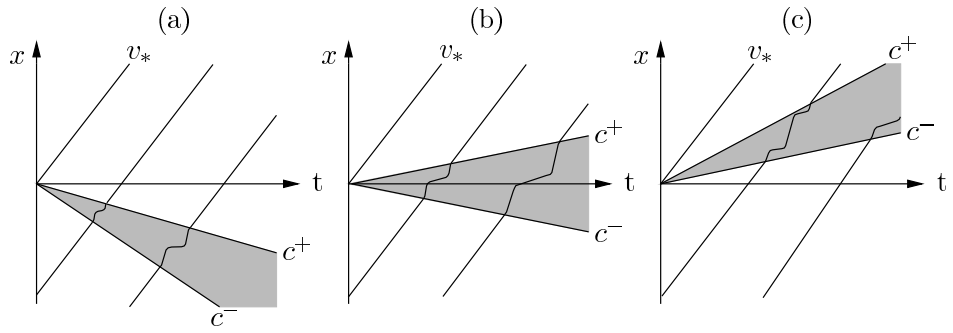

Figure 2. Illustration of vehicle trajectories with equilibrium velocity v_* in (x, t) space for upstream convective instability (a), absolute instability (b) and downstream convective instability (c). The wedges of growing instability are shaded in grey and bounded up and downstream by the velocities c^- and c^+ respectively.

Treiber *et al.* (2000, 2010), but so far a full mathematical analysis has been lacking.

In this paper we present rigorous mathematical criteria that distinguish been convective string instability and absolute string instability in the road frame. The calculations are developed for a general family of car-following models introduced in §2. The basis structure of the linearisation is then explained in §3. The chief idea is to calculate ranges of wave speeds that correspond to the propagation of *information*. The calculations that then follow are of two types:

- Firstly (§4), we compute the *group velocity* that can be supported by growing modes. This work is thus a generalisation of Mitarai & Nakanishi (2000) who computed group velocity for a particular car-following model known as the Optimal Velocity model. More recent work by Helbing & Johansson (2009) revisited the Optimal Velocity model and in addition computed the group velocity for a family of related macroscopic (partial differential equation) models. All of these group velocity calculations are attractive because they are simple both conceptually and in terms of their mathematical details. However, this approach is based on the flawed assumption that *group velocity* is equivalent to the *velocity of information* — when, in fact, this assumption is true only for non-dissipative media (Brillouin, 1960).

- The correct approach (§5) employs the calculation of *signal velocity*, which may be defined loosely as the velocity at which a new signal can penetrate a medium which is at rest. This calculation employs the steepest-descent method to determine the large-time asymptotics of the vehicle trajectories. This leads to an intriguing mathematical problem concerning the saddle selection procedure that is described in detail in Appendix B.

Unfortunately (from the point of view of the practitioner), the extra complication of the signal velocity calculation is required, because the group velocity and signal velocity are only the same for non-dissipative media (Brillouin, 1960). For example, in light propagation, it is know that dissipative media may exhibit superluminal group velocity (Garrett & McCumber, 1970; Wang *et al.*, 2000).

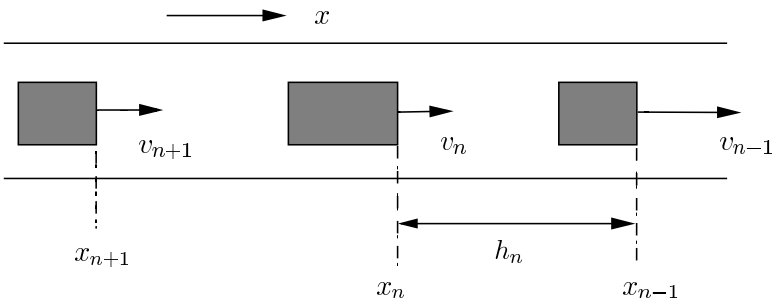

Figure 3. Car-following model set-up, see equation (2.2).

Section 6 gives numerical results for two particular examples of car-following models. In particular, figure 1 suggests that in congested conditions, information should propagate only upstream in the road frame, and hence we seek models and parametrisations which replicate this behaviour. In fact, the absence of downstream growth in macroscopic data is not incompatible with convective downstream or absolute *linear* instability, if it is combined with more complicated model features. For example, one might try to construct set-ups in which the downstream growth is trapped at junctions by the spatial heterogeneity of the road, and where the consequent upstream propagation results from nonlinear effects.

However, in the parsimonious framework that we consider, it is a sensible starting point to require that models display only convective upstream linear instability in the road frame. As we shall see, this is a rather strong criterion in model parametrisation, which not all models obey for all parameter values. This practical theme is taken up further in §7, where conclusions and opportunities for further work are presented.

2. Modelling details

We follow the general car-following model framework developed in Wilson (2008). Our starting point is the standard situation depicted in figure 3. We consider a single lane of traffic with identical vehicles labelled 1, 2, etc., in the upstream direction. Displacements and velocities are denoted $x_n(t)$ and $v_n(t) \geq 0$ respectively, and our models shall also involve the front-to-front spacing $h_n(t) := x_{n-1}(t) - x_n(t) > 0$ of consecutive vehicles, sometimes referred to as the headway. Note that overtaking is neglected in our framework in return for analytical tractability, and our approach is to view lane-changes (and other imperfections, such as noise, heterogeneous road, differences between drivers etc.) as external perturbations to a deterministic single lane model whose stability should then be analysed.

In their simplest form, car-following models consist of a set of coupled differential equations for the trajectory of each vehicle, which supplements the kinematic relations

$$\dot{x}_n = v_n, \tag{2.1}$$

with a behavioural model

$$\dot{v}_n = f(h_n, \dot{h}_n, v_n). \tag{2.2}$$

Here dot denotes differentiation with respect to time, and equation (2.2) mimics how drivers accelerate or decelerate in response to the distance to the vehicle in front, the relative velocity

$$\dot{h}_n = v_{n-1} - v_n, \tag{2.3}$$

and their own velocity. The point of this paper is to derive results for models in the general form of equation (2.2) with the minimum number of additional assumptions. However, to demonstrate the theory in operation, we illustrate the paper with two representative examples:

1. The OVRV (Optimal Velocity with Relative Velocity) model, see Jiang *et al.* (2001); Ward (2008). We have

$$f(h_n, \dot{h}_n, v_n) = \alpha \left(V(h_n) - v_n \right) + \beta \dot{h}_n, \tag{2.4}$$

   where V is the so-called Optimal Velocity function defining the maximum safe speed for a given headway, which drivers relax towards at rate $\alpha > 0$. The term $\beta \dot{h}_n$ ($\beta > 0$) models the tendency for drivers to brake when closing in on their predecessor, and to accelerate when the gap is increasing. The OVRV model is not intended to model quantitative details of driver behaviour, but rather to capture the correct qualitative features in the simplest possible functional form. When $\beta = 0$, the OVRV model reduces to the much-studied Optimal Velocity model due to Bando *et al.* (1995). We will follow Bando *et al.* (1995) and work in dimensionless variables with the choice

$$V(h) = \tanh(2) + \tanh(h - 2). \tag{2.5}$$

2. The Intelligent Driver Model (IDM), see Treiber *et al.* (2000). We have

$$f(h, \dot{h}, v) = a \left[1 - \left(\frac{v}{v_0} \right)^{\delta} - \left(\frac{s^*(v, \dot{h})}{h - l} \right)^2 \right], \tag{2.6}$$

   where

$$s^*(v, \dot{h}) := s_0 + s_1 \sqrt{\frac{v}{v_0}} + \tau v - \frac{v \dot{h}}{2\sqrt{ab}}, \tag{2.7}$$

   and the notation and standard parameter values are given in table 1. In contrast to the OVRV model, the IDM is an attempt to model driver behaviour quantitatively in dimensional terms, and we may view equations (2.6,2.7) as a proxy for the complicated schemes that one usually finds in commercial microsimulation packages.

Note in practice there are many possible refinements to equation (2.2) such as the inclusion of reaction-time delay, multi-anticipation (where the motion of more than one vehicle ahead is considered), lane-changing effects, and heterogeneity of the vehicle fleet and driver population — but these are beyond the scope of this paper: see Brackstone & McDonald (1999); Helbing (2001) for reviews.

Table 1. *IDM parameter values*

Parameters		Dimensional values
Desired velocity,	v_0	120 km/h (33.33 m s^{-1})
Safe time headway,	τ	1.6 s
Max. acceleration,	a	0.73 m s^{-2}
Desired deceleration,	b	1.67 m s^{-2}
Acceleration exponent,	δ	4
Jam distance,	s_0	2 m
Jam distance,	s_1	0 m
Vehicle length,	l	5 m

3. Uniform flow and linear stability preliminaries

Motivated by data, we focus on models described by equation (2.2) that have an equilibrium speed-headway function V such that

$$f(h_*, 0, V(h_*)) = 0 \quad \text{for all} \quad h_* > 0. \tag{3.1}$$

In some models, such as the OVRV (see equation (2.4)), the function V is provided explicitly as a parameter, whereas in others, such as the IDM (see equations (2.6,2.7)) it is derived by isolating v_* from the relation $f(h_*, 0, v_*) = 0$. Whichever is the case, we require that V satisfies: 1. $V(0) = 0$, 2. $V' \geq 0$ and 3. $V(h) \to V_{\max}$ as $h \to \infty$.

The consequence of equation (3.1) is a one-parameter family of steady driving solutions known as *uniform flows*, in which $x_n(t) = x_0 - nh_* + tV(h_*)$. Thus in a uniform flow solution, all vehicles drive at the same speed $V(h_*)$ (so that the relative velocity of any pair of vehicles is zero) with the same time-independent headway h_*. In the t-x plane, vehicle trajectories are thus equally spaced parallel straight lines.

Our approach is to consider small perturbations to the uniform flow equilibria by setting $h_n = h_* + \tilde{h}_n(t)$ and $v_n = V(h_*) + \tilde{v}_n(t)$, where $\tilde{h}_n$ and $\tilde{v}_n$ are small. Assuming f is sufficiently smooth, this linearisation yields

$$\dot{\tilde{v}}_n = f_h \tilde{h}_n + f_{\dot{h}} \dot{\tilde{h}}_n + f_v \tilde{v}_n, \tag{3.2}$$

where the partial derivatives are evaluated at the constant equilibrium arguments $(h_*, 0, V(h_*))$, and necessary constraints for rational driver behaviour are

$$f_h,\ f_{\dot{h}} > 0 \quad \text{and} \quad f_v < 0. \tag{3.3}$$

These conditions simply state that drivers increase their acceleration in response to an increase in headway or relative velocity but tend to decrease their acceleration as their own velocity increases. At very large headway, the sensitivity of the dynamics to the vehicle in front is very slight, so we should also allow f_h, $f_{\dot{h}} = 0$. However, since the focus of our stability calculations is on close-following situations, we shall maintain strict inequality in equation (3.3).

Since equation (2.3) implies $\dot{\tilde{h}}_n = \tilde{v}_{n-1} - \tilde{v}_n$ and $\ddot{\tilde{h}}_n = \dot{\tilde{v}}_{n-1} - \dot{\tilde{v}}_n$, we may apply the difference operator to equation (3.2) to obtain

$$\ddot{\tilde{h}}_n + (f_{\dot{h}} - f_v)\dot{\tilde{h}}_n + f_h \tilde{h}_n = f_{\dot{h}} \dot{\tilde{h}}_{n-1} + f_h \tilde{h}_{n-1}, \tag{3.4}$$

which is the key equation in this paper. Fundamentally, equation (3.4) describes the second order dynamics of vehicle n driven by those of vehicle $n-1$ ahead of it. We stress that in this modelling framework, perturbations can only propagate *upstream* relative to the vehicle frame, however it remains an open question as to which direction disturbances propagate relative to the road frame.

Let us consider the the left-hand side differential operator of equation (3.4). Its characteristic equation (cf Kesting & Treiber (2008)) is

$$\mu^2 + (f_{\dot{h}} - f_v)\mu + f_h = 0. \tag{3.5}$$

Since all coefficients are positive (by equation (3.3)), the roots (that we call *platoon eigenvalues*) are either complex conjugate with negative real parts, or both real and negative. Hence the differential operator is stable. The consequence is that if an instantaneous perturbation is applied to a finite platoon of vehicles whose leader's velocity is held fixed, then as $t \to \infty$, every vehicle returns to equilibrium. Hence the models that we consider do not exhibit *platoon instability* (sometimes referred to as *local instability* in the classical traffic literature).

However, the key point is that a platoon-stable model can nevertheless display instability when observed in a moving frame of reference. This is the essential point of *convective instability*, also known as *string instability* in the classical traffic literature. To understand this point, consider a semi-infinite column of vehicles in uniform flow whose leader drives at a fixed speed. Let us suppose that the second vehicle in the column is instantaneously 'kicked' out of equilibrium, and let us study the ensuing fluctuations which propagate back up the column of vehicles. Each vehicle in turn will be disturbed momentarily from equilibrium, but then return to steady driving owing to *platoon stability*. However, if the column is *string-unstable*, the maximum departure from equilibrium that each vehicle experiences will increase as one goes further and further up the column of vehicles. See Wilson & Ward (2010) for a more detailed discussion of this process.

4. Group velocity calculations

Our first attempt at understanding string instability is a development of the general Fourier analysis presented in Wilson (2008). The point is to solve equation (3.4) via the ansatz

$$\tilde{h}_n = \mathrm{Re}\left(A\mathrm{e}^{\mathrm{i}n\theta}\mathrm{e}^{\lambda t}\right), \tag{4.1}$$

which yields the quadratic characteristic equation

$$\lambda^2 + \left\{f_{\dot{h}}(1-\mathrm{e}^{-\mathrm{i}\theta}) - f_v\right\}\lambda + f_h(1-\mathrm{e}^{-\mathrm{i}\theta}) = 0, \tag{4.2}$$

to solve for the (generally complex) growth rate λ in terms of the discrete wavenumber θ, $0 < \theta \leq \pi$. Here a small (positive) value of θ corresponds to very long wavelength fluctuations, and $\theta = \pi$ gives the shortest possible wavelength in this discrete setting, i.e., a perturbation that is period-two in the vehicle index. The solutions to equation (4.2) are given exactly by

$$\lambda_{\pm}(\theta) = \frac{1}{2}\left\{ - \left[f_{\dot{h}}\left(1-\mathrm{e}^{-i\theta}\right) - f_v\right] \pm \sqrt{\left[f_{\dot{h}}\left(1-\mathrm{e}^{-i\theta}\right) - f_v\right]^2 - 4f_h\left(1-\mathrm{e}^{-i\theta}\right)}\right\}, \tag{4.3}$$

where stability of a given mode is governed by the root λ_+ with greatest real part. In Wilson (2008) it is proven that if any given wavenumber θ is unstable, i.e., if $\lambda_{\rm r}(\theta) := {\rm Re}(\lambda_+(\theta)) > 0$, then all smaller wavenumbers (i.e., longer wavelengths) are unstable too — in the sense that $\lambda_{\rm r}(\tilde{\theta}) > 0$ for $0 < \tilde{\theta} < \theta$. Hence stability of a given uniform flow solution is controlled by long wavelengths in that one only need test the sign of $\lambda_{\rm r}(0+)$.

From equation (4.2) we have $\lambda(-\theta) = \overline{\lambda(\theta)}$ and hence that the real and imaginary parts of λ are even and odd functions of θ respectively. Thus we seek the expansion

$$\lambda_+ = i\lambda_1\theta + \lambda_2\theta^2 + i\lambda_3\theta^3 + \lambda_4\theta^4 + \ldots, \tag{4.4}$$

with real coefficients λ_1, λ_2, ..., etc. Here the sign of the real part

$$\lambda_{\rm r}(\theta) = \lambda_2\theta^2 + \lambda_4\theta^4 + \ldots \tag{4.5}$$

governs whether a given mode grows or decays, and we define

$$\omega(\theta) := -{\rm Im}(\lambda_+(\theta)), \qquad = -\lambda_1\theta - \lambda_3\theta^3 - \ldots, \tag{4.6}$$

so that $\omega(\theta)/\theta$ gives the phase velocity measured relative to the discrete lattice coordinate, with a positive value denoting upstream propagation.

By equating powers of θ in equation (4.2), we find

$$\lambda_1 = \frac{f_h}{f_v}, \quad = -V'(h_*) < 0, \tag{4.7}$$

and

$$\lambda_2 = \frac{f_h}{f_v^3}\left(\frac{f_v^2}{2} - f_{\dot{h}}f_v - f_h\right). \tag{4.8}$$

Note the sign of $\lambda_{\rm r}(0+)$ is given by the sign of λ_2, which thus gives the bifurcation condition (Wilson, 2008). Precisely:

- For $\lambda_2 < 0$, the given uniform flow is linearly stable in that all wavenumbers are linearly stable.
- For $\lambda_2 > 0$, the given uniform flow is linearly unstable to small wavenumber (long wavelength) modes, and we may speak of a *window* of instability, i.e. a range $0 < \theta < \theta_{\rm max}$ of unstable wavenumbers for which $\lambda_{\rm r}(\theta) > 0$.

Plots of $\lambda_{\rm r}(\theta)$ for the stable and unstable cases are displayed in figure 4.

When a uniform flow is only marginally unstable, the window of instability is confined to relatively small wavenumbers. In this case, $\lambda_{\rm r}(\theta)$ is well approximated by the first two terms in its series, see equation (4.5). Since it may be shown that $\lambda_4 < 0$ when $\lambda_2 > 0$ (see Appendix A), it follows that

$$\theta_{\rm max} \simeq \theta_{\rm max}^{\rm approx} := \sqrt{-\lambda_2/\lambda_4}. \tag{4.9}$$

However, the exact value of $\theta_{\rm max}$ may also be calculated numerically from equation (4.3).

The point now is to determine the speed of *packets* of waves (focusing later on unstable modes for which $\lambda_{\rm r}(\theta) > 0$). In the lattice frame (i.e., relative to the

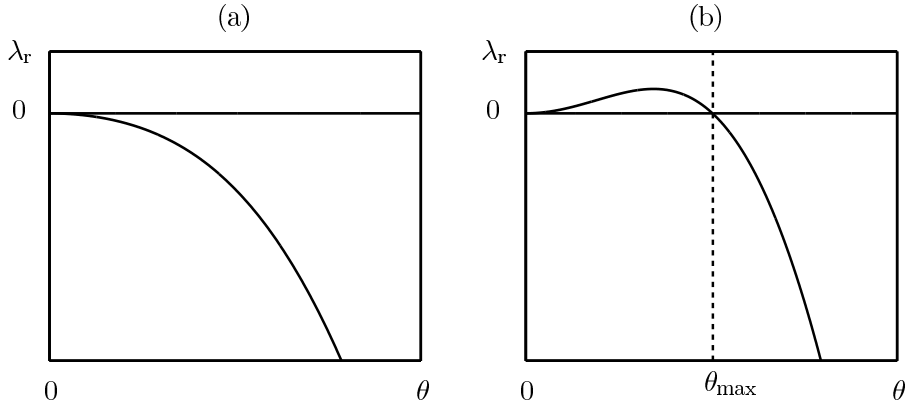

Figure 4. Growth rate λ_r as a function of discrete wavenumber θ: (a) stable; (b) unstable. The transition to instability is given by a change in the sign of the second derivative λ_2 at $\theta = 0$. Observe that $\lambda_r = 0$ when $\theta = 0$ because of neutral stability within the continuous family of uniform flow solutions.

column of vehicles), the upstream speed of a packet of wavenumber θ is given by the well-known group velocity $\omega'(\theta) = \mathrm{d}\omega/\mathrm{d}\theta$, which must be multiplied by the underlying lattice spacing h_* to give a dimensional speed. However, since vehicles (i.e., the lattice points) are moving downstream with the underlying velocity $V(h_*)$, the velocity of the wave packet relative to the road frame is given by

$$c_g(\theta) := V(h_*) - h_*\omega'(\theta), \tag{4.10}$$

where a positive (resp. negative) value denotes downstream (resp. upstream) propagation. Henceforth we refer to $c_g(\theta)$ defined by equation (4.10) as simply *the* group velocity.

To calculate $c_g(\theta)$ exactly, we need to differentiate the quadratic formula in equation (4.3) directly. However, for small θ we may alternatively use equation (4.7) and the first two terms of equation (4.6) to obtain

$$c_g(\theta) \simeq [V(h_*) + h_*V'(h_*)] + 3h_*\lambda_3\theta^2. \tag{4.11}$$

Since it may be shown that $\lambda_3 > 0$ when $\lambda_2 > 0$ (see Appendix A), it follows that $c_g(\theta)$ is an increasing function for small θ. In fact, $c_g(\theta)$ is increasing for all θ, but the proof requires the direct differentiation of equation (4.3) (details omitted here).

We now return to the fundamental question, namely how to classify the instability of uniform flow. The approach that we take here is to view the group velocity $c_g(\theta)$ as a proxy for the velocity of propagation of information. In fact, as we have discussed, this approach is flawed, because the traffic models that we consider are not non-dissipative and so instead the *signal velocity* should be used. (This is a more difficult calculation that follows in §5.)

However, for the time being, we identify the range of group velocities exhibited by unstable wavenumbers, and consequently the range of velocities with which wave packets can be propagated without decay. Specifically, we take an unstable uniform flow (for which $\lambda_2 > 0$) and define

$$c_g^- := \inf\{c_g(\theta) : 0 < \theta < \theta_{max}\} \quad \text{and} \quad c_g^+ := \sup\{c_g(\theta) : 0 < \theta < \theta_{max}\}. \tag{4.12}$$

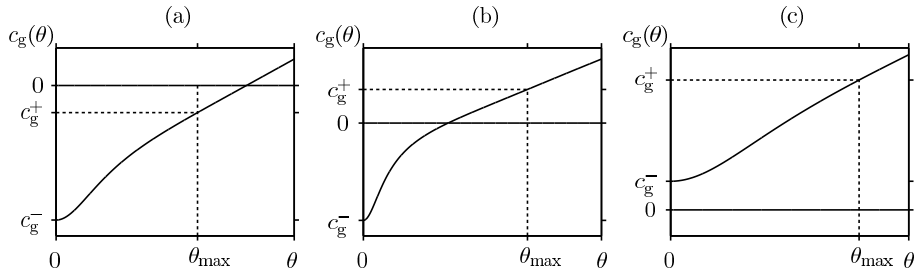

Figure 5. Illustration of how the group velocity $c_g(\theta)$ may be used to identify convective and absolute instabilities. The leading and trailing edge velocities, $c_g^+ = c_g(\theta_{max})$ and $c_g^- = c_g(0)$ respectively, are labelled. In panel (a), both c_g^+ and c_g^- are negative, thus the disturbance travels upstream against the flow of traffic and is convective. In panel (b) c_g^+ is positive and c_g^- is negative and hence the disturbance travels simultaneously up and downstream and is absolutely unstable. Panel (c) is convectively unstable because both c_g^+ and c_g^- are positive.

In some sense, c_g^- and c_g^+ thus capture respectively the velocities of the upstream and downstream edges of the wedge of instability (see figure 2). The three types of instability are then characterised as follows:

- $c_g^- < c_g^+ < 0$. Convective upstream instability. (Wave packets only propagate upstream.)
- $c_g^- < 0 < c_g^+$. Absolute instability. (Wave packets propagate in both directions.)
- $0 < c_g^- < c_g^+$. Convective downstream instability. (Wave packets propagate only downstream.)

This classification is depicted in the numerical examples in figure 5. Because $c_g(\theta)$ is an increasing function, it follows that

$$c_g^- = c_g(0) \quad \text{and} \quad c_g^+ = c_g(\theta_{max}). \tag{4.13}$$

Thus we have the exact formula

$$c_g^- = V(h_*) + h_* V'(h_*), \tag{4.14}$$

but the exact calculation of c_g^+ requires the application of numerical methods to equation (4.3), to calculate θ_{max} and the derivative ω'. However, for cases which are only marginally unstable, in that θ_{max} is small, we may use equation (4.9) in combination with equation (4.11) to obtain

$$c_g^+ \simeq c_g^- - 3h_* \frac{\lambda_2 \lambda_3}{\lambda_4}. \tag{4.15}$$

The analytical details of the group velocity calculation are now complete. Later, in §6, we classify whole ranges of uniform flows for the exemplar models introduced in §2, and in particular we chart how the stability changes with parameters. This process involves calculating the transitions between absolute and convective upstream (resp. downstream) instability defined by the locus of $c_g^+ = 0$ (resp. $c_g^- = 0$).

5. Signal velocity calculations

So far we have used the group velocity (which characterises the propagation of wave packets) in order to classify instability in the linearised general car-following model defined in equation (2.2). We now use asymptotic methods to calculate the *signal velocity*, at which information penetrates a medium that is initially at rest (Brillouin, 1960). As we have discussed, the group velocity and signal velocity are usually different. The group velocity is found by a simpler calculation, but it is the signal velocity which correctly represents the propagation of information.

Our set-up is a notional experiment in which a semi-infinite column of vehicles $n \geq 0$ are given equilibrium initial data $h_n(0) = h_*$ and $v_n(0) = V(h_*)$. We then prescribe a small disturbance to the trajectory of the lead vehicle $n = 0$, which is localised in time, and we examine how this perturbation drives the motion of the vehicles upstream. Thus for $n \geq 1$ we take the Laplace transform of equation (3.4) and obtain

$$\left[z^2 + (f_{\dot{h}} - f_v)z + f_h\right] F_n(z) = \left[f_{\dot{h}} z + f_h\right] F_{n-1}(z), \tag{5.1}$$

where $F_n(z)$ denotes the Laplace transform of $\tilde{h}_n(t)$. This recursion relation can be solved to yield

$$F_n(z) = g(z)^n F_0(z), \tag{5.2}$$

where

$$g(z) = \frac{f_{\dot{h}} z + f_h}{z^2 + (f_{\dot{h}} - f_v)z + f_h}. \tag{5.3}$$

For $n \geq 1$, we apply the Laplace inversion formula

$$\tilde{h}_n(t) = \frac{1}{2\pi \mathrm{i}} \int_{\gamma - \mathrm{i}\infty}^{\gamma + \mathrm{i}\infty} g(z)^n F_0(z) \mathrm{e}^{tz} \mathrm{d}z, \tag{5.4}$$

where γ is chosen to the right of the poles of $g(z)$, given by the *platoon eigenvalues* μ that solve equation (3.5). In fact, this integral can be solved explicitly by calculating the residue at the poles, but since these are degree n, we must apply the Leibnitz formula to compute the $(n-1)$-th derivative of the regular part of the integrand. This procedure is tractable but yields a complicated double sum which cannot be analysed further.

Hence instead we analyse equation (5.4) by asymptotic methods. Our approach is to apply the *method of steepest descents* to equation (5.4) to extract the $t \to \infty$ behaviour: see Bender & Orszag (1999, Chap. 6) for details. The general scope of the method is the integral

$$I = \int_{\mathcal{C}} f(z) \exp(t\rho(z)) \, \mathrm{d}z, \tag{5.5}$$

where $f(z)$ and $\rho(z)$ are analytic except at isolated singularities (poles, branch cuts etc.). The idea is then to consider an alternative contour $\mathcal{C}'$ which is obtained by deforming $\mathcal{C}$. If this can be achieved without crossing the integrand's singularities, then I is unchanged by Cauchy's theorem. We seek such a $\mathcal{C}'$ that passes through a saddle point z_* at which $\rho'(z_*) = 0$, and at which is attained the local and global maxima of $\mathrm{Re}(\rho(z))$ along the contour. In consequence, as $t \to \infty$, the local

properties of the integrand at the saddle point dominate the integral, and the leading order asymptotics may be computed in the form

$$I \sim \left(\sqrt{\frac{2\pi}{t|\rho''(z_*)|}} \right) f(z_*) \exp\left(t\mathrm{Re}\rho(z_*)\right) \exp\left(\mathrm{i}(\zeta + t\mathrm{Im}(\rho(z_*)))\right), \tag{5.6}$$

where $\zeta = \arg \rho''(z_*)/2 + \pi/2$.

In its present form, the integral (5.4) gives $\rho(z) = z$, and consequently there is no saddle point. The trick is thus to write the integrand in the form

$$g(z)^n F_0(z) \mathrm{e}^{tz} = F_0(z) \exp\left(tz + n \log g(z)\right), \tag{5.7}$$

so that we may proceed with $f(z) = F_0(z)$ and

$$\rho(z) = z + \kappa \log g(z), \tag{5.8}$$

where $\kappa = n/t$. For the method of steepest descents to work, we require $\rho(z)$ and $f(z)$ to be independent of t, so we fix κ while we apply the $t \to \infty$ asymptotics. In essence, we thus analyse wave propagation along a ray with speed κ upstream in the lattice frame.

To clarify the structure of the calculation: we have $\tilde{h}_n(t) = I/2\pi\mathrm{i}$, where I is given asymptotically (for large t) by (5.6). In equation (5.6), the saddle point z_* is a function of $\kappa = n/t$, which is found by the procedure that we now develop.

The saddle points are found by computing

$$\rho'(z) = 1 + \kappa \frac{g'(z)}{g(z)}, \tag{5.9}$$

and thus we seek solutions of

$$g(z) + \kappa g'(z) = 0, \tag{5.10}$$

yielding the cubic equation

$$f_{\dot{h}} z^3 + \left[f_h + f_{\dot{h}}(f_{\dot{h}} - f_v) - f_{\dot{h}}\kappa\right] z^2 + \left[f_h f_{\dot{h}} + f_h(f_{\dot{h}} - f_v) - 2f_h\kappa\right] z + f_h^2 + f_h f_v \kappa = 0, \tag{5.11}$$

parametrised by κ.

In general, equation (5.11) must be solved numerically. The question is then for a given κ, which of the three roots of equation (5.11) should be taken as z_* in formula (5.6). The requirements are that 1. the saddle point in question is a local maximum (rather than a local minimum) of $\mathrm{Re}(\rho(z))$ in the direction of the contour; 2. that it is also the *global* maximum of $\mathrm{Re}(\rho(z))$ on the contour; and 3. that the contour may be obtained by deformation of the line $(\gamma - \mathrm{i}\infty, \gamma + \mathrm{i}\infty)$ without crossing the poles of $g(z)$ (i.e., the platoon eigenvalues μ). These requirements concern the level set geometry of $\mathrm{Re}(\rho(z))$ which is considered in detail in Appendix B.

The selection procedure developed in Appendix B has some delicate features for small κ which nevertheless may be automated by computer. However, for $\kappa > 0.1\sqrt{f_h}$, the following particularly simple prescription holds:

Case 1. Equation (5.11) has one real and two complex conjugate roots. The two complex conjugate roots are the saddles z_* of interest and the contour should

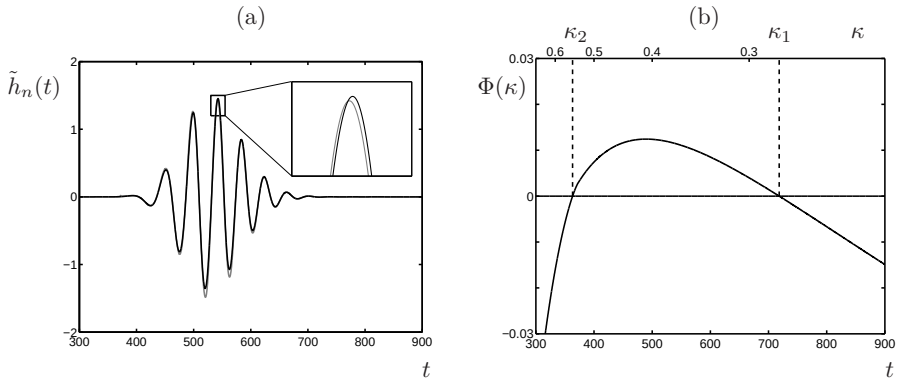

Figure 6. In panel (a) we compare the asymptotic expansion (grey) and microscopic simulation data (black) for the IDM model with standard parameter values (see table 1) at the equilibrium velocity $v_* = 10\,\mathrm{ms}^{-1}$. The lead vehicle has a fixed constant speed and instability is triggered by increasing the initial velocity of the second vehicle by 0.5% above the equilibrium value. The perturbation field $\tilde{h}_n(t)$ of vehicle $n = 200$ is plotted against time t. The asymptotic expansion is calculated from equation (5.6) over a range of values of $\kappa = n/t$. A close up of the comparison is plotted in the inset. In panel (b) we plot the corresponding exponential growth factor $\Phi(\kappa)$ for the asymptotic results presented in panel (a). The time scale is plotted linearly on the lower horizontal axis, as in panel (a), and the corresponding values of κ are labelled on the upper horizontal axis. The critical speeds, κ_1 and κ_2, bounding the envelope of the disturbance, are marked with dashed lines.

be deformed over both, to incorporate two terms of the form of equation (5.6). However, each complex conjugate contributes the same exponential growth factor, so that either may be used in the criterion that follows.

Case 2. Equation (5.11) has three real roots. The greatest, i.e., $z_* = \max(z_1, z_2, z_3)$ is the one of interest.

Once the correct saddle $z_*(\kappa)$ has been selected, formula (5.6) may be used to derive the $t \to \infty$ asymptotics of $\tilde{h}_n(t)$ as we have described above. Note that this procedure gives rise automatically to a real answer for $\tilde{h}_n(t)$. In case 2., this is because the saddle in question is real, whereas in case 1. it is due to cancellation of the conjugate components from the pair of saddles that is used.

Figure 6(a) shows an example of just how close the asymptotic agreement is. However, more importantly, we may extract the dominating exponential growth factor from equation (5.6), in the form

$$\Phi(\kappa) := \phi(z_*(\kappa)), \tag{5.12}$$

where

$$\phi(z) := \mathrm{Re}(\rho(z)) = \mathrm{Re}(z) + \kappa \log|g(z)|. \tag{5.13}$$

If $\Phi(\kappa) > 0$, then perturbations grow along the ray in question, whereas if $\Phi(\kappa) < 0$, they decay.

The next task is to consider how Φ depends on κ. We have no proofs as to the general structure, but rather we use a numerical procedure which loops over κ, solving the cubic equation (5.11) and selecting the correct saddle for each individual

value of κ. A typical computation is illustrated in figure 6(b). In general, for linearly unstable uniform flows, we find κ_1, $\kappa_2 > 0$ such that $\Phi(\kappa) > 0$ for $\kappa_1 < \kappa < \kappa_2$, and $\Phi(\kappa) < 0$ elsewhere. Thus κ_1 and κ_2 identify critical speeds bounding a wedge in which perturbations grow. Thus we may establish signal velocities

$$c_{\rm s}^- := V(h_*) - \kappa_2 h_* \quad \text{and} \quad c_{\rm s}^+ := V(h_*) - \kappa_1 h_*, \tag{5.14}$$

measured relative to the road frame, which bound the envelope in which perturbations grow. The signs of the signal velocities $c_{\rm s}^-$ and $c_{\rm s}^+$ may then be analysed in the same way as those of the group velocities $c_{\rm g}^-$ and $c_{\rm g}^+$ (§4) in order to classify the type of stability.

6. Examples and illustrations

So far, in §4 and §5, we have developed general analytical methods in order to establish a recipe that can be used to classify the stability of any car-following model that complies with the general formulation (2.2). To illustrate what may be achieved, we now apply these techniques to the exemplar models introduced in §2.

Note that it is no longer sufficient to study the stability of a single uniform flow solution. Rather, a car-following model should be characterised by analysing the stability class of *all* of its uniform flow solutions, as the equilibrium headway (or velocity) and the model parameters are varied.

To begin with, we fix the model parameters by choosing (a) $\alpha = 0.6$ and $\beta = 0.2$ for the OVRV model and (b) by selecting the standard published parameters for the IDM model (table 1). We then scan through a range of equilibrium velocities v_* and compute the corresponding bounding group velocities $c_{\rm g}^\pm$ (§4) and signal velocities $c_{\rm s}^\pm$ (§5).

See figures 7(a,b) for the results. In each plot we observe 'bubbles' formed by the pairs of curves $(c_{\rm g}^-, c_{\rm g}^+)$ and $(c_{\rm s}^-, c_{\rm s}^+)$ which mark the extent of the unstable regime. Note that in general the group velocities and signal velocities do not agree, except at the left- and right-hand edges of the bubbles which correspond to the onset of instability — at which points the underlying linear models are non-dissipative.

Furthermore, in figures 7(a,b) we classify ranges of equilibrium velocity v_* according to the bounding signal velocities, so that

1. $\rm C_u$ (convective upstream instability) corresponds to $c_{\rm s}^- < c_{\rm s}^+ < 0$;
2. A (absolute instability) corresponds to $c_{\rm s}^- < 0 < c_{\rm s}^+$; and
3. $\rm C_d$ (convective downstream instability) corresponds to $0 < c_{\rm s}^- < c_{\rm s}^+$.

In the unshaded ranges labelled S, the dynamics are linearly stable because $\lambda_2 < 0$, see equation (4.8).

When traffic is unstable, we find

$$c_{\rm g}^- < c_{\rm s}^- < c_{\rm g}^+ < c_{\rm s}^+, \tag{6.1}$$

and we conjecture that this is a general result. In consequence, the range $(c_{\rm s}^-, c_{\rm s}^+)$ of possible signal velocities overlaps but is downstream of the range $(c_{\rm g}^-, c_{\rm g}^+)$ of possible group velocities. Extreme caution is thus required if group velocity is used as a

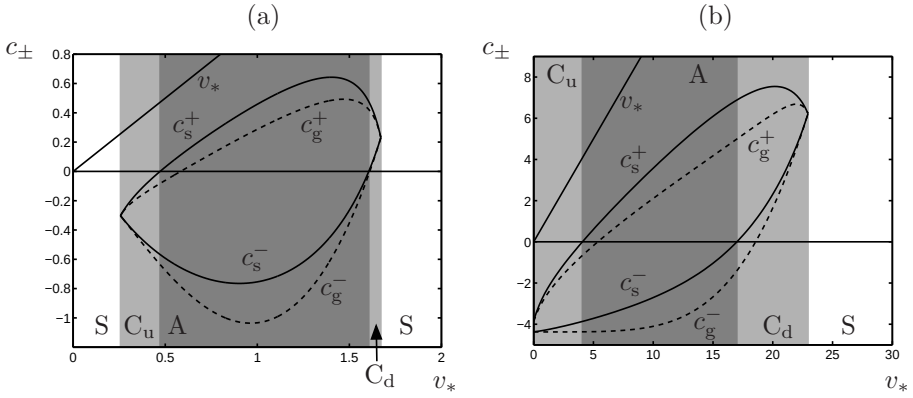

Figure 7. Comparison of the bounding group $c_g^\pm$ and signal velocities $c_s^\pm$ as the equilibrium velocity v_* is varied. The OVRV model with parameters $\alpha = 0.6$ and $\beta = 0.2$ is used in panel (a) and the IDM model with standard parameter values (see table 1) is used in panel (b). Here S denotes stable dynamics and instability is classified according to the signal velocities: C_u denotes convective upstream instability; A denotes absolute instability; and C_u denotes convective downstream instability. Note that all wave propagation velocities are less than the traffic equilibrium velocity v_*, because information always propagates upstream relative to the vehicles.

proxy for the propagation of information. In particular, a model may be considered 'good' from the point of view of group velocity, in that $c_g^- < c_g^+ < 0$ and thus downstream propagation in the road frame appears to be avoided. However, one may have $c_s^+ > 0$ so that instability is in fact absolute.

To investigate the classification of instability further, we now compute two-parameter diagrams in which both the equilibrium velocity and a single model parameter are varied. For the latter (and for the purposes of illustration), we choose the sensitivity parameters, namely α in the OVRV model (see equations (2.4,2.5)) and a in the IDM model (see equations (2.6,2.7)).

See figure 8 for the results, where the regimes are computed and labelled according to the signal velocity, in the same way as for the one-parameter pictures in figure 7. The boundaries between the different instability regions (denoted by solid lines) are thus computed by tracing out the loci of $c_s^- = 0$ and $c_s^+ = 0$. In addition, dashed lines show the loci of $c_g^- = 0$ and $c_g^+ = 0$, so that it is clear that using the group velocity will not achieve the same classification as using the signal velocity. The boundary of the stable regime S is found by computing the locus of $\lambda_2 = 0$.

Note that figure 8 establishes that the stability charts for the OVRV model and the IDM are qualitatively the same. We have found that most 'reasonable' car-following models seem to generate similar pictures, but this assertion can only be supported by a much more detailed numerical study that is beyond the scope of this paper.

As we have discussed, we consider it appropriate that practical car-following models are parametrised so that linear stability is only ever convective upstream (type C_u) in the road frame. However, in the IDM model, the standard choice $a = 0.73\text{m/s}^2$, indicated by the horizontal dotted line in figure 8(b), attains all 3 types of instability. Thus our analysis suggests that a larger value, e.g., $a \simeq 1.2\text{m/s}^2$ is better.

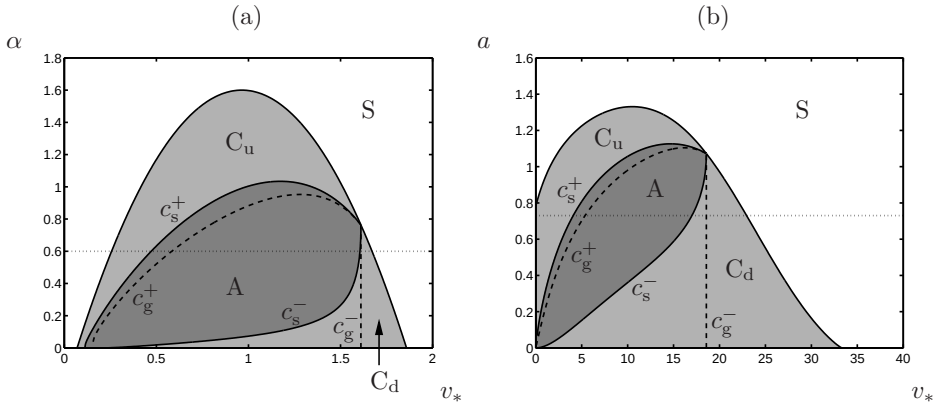

Figure 8. Classification of the stability regions for (a) the OVRV model (with $\beta = 0.2$) and (b) the IDM model (standard parameters from table 1). We vary the sensitivity parameters α and a respectively, and consider the stability of uniform flows parametrised by the equilibrium velocity v_* (in order to compress the horizontal axis). The horizontal dotted lines ($\alpha = 0.6$ and $a = 0.73$ in panels (a) and (b) respectively) denote the one-dimensional sections which were explored in figure 7. As for figure 7, S denotes stable dynamics and instability is classified according to the signal velocities: $\mathrm{C_u}$ denotes convective upstream instability; A denotes absolute instability; and $\mathrm{C_d}$ denotes convective downstream instability. The solid lines labelled $c_{\mathrm{s}}^{\pm}$ denote the loci $c_{\mathrm{s}}^{\pm} = 0$ and hence the boundaries of the different instability regions. The dashed lines labelled $c_{\mathrm{g}}^{\pm}$ denote the loci $c_{\mathrm{g}}^{\pm} = 0$ and hence indicate how the classification would change if computed according to the group velocity.

In fact, in figure 8 we may observe that as the sensitivity parameter (α or a) is reduced, the onset of instability is *convective upstream*, i.e., the desirable kind of instability. Only when the sensitivity parameter is reduced much further do we also obtain (undesirable) absolute and convective downstream instability. This suggests that when parametrising microsimulation models, one should generally choose parameters which are only slightly unstable at the linear level, so that only type $\mathrm{C_u}$ instability is obtained.

Why is the onset of instability (as α or a is reduced) convective? Recall (figure 7) that at onset, the bounding signal and group velocities coincide so that the group velocity classifies the type of instability correctly. Further, at onset, $\theta_{\max} = 0+$, so that $c_{\mathrm{g}}^{+} = c_{\mathrm{g}}(0+) = c_{\mathrm{g}}^{-}$ from equation (4.13). Thus there is a single value of group velocity (rather than an admissible window) and instability is thus convective upstream (resp. downstream) if the group velocity is negative (resp. positive). To distinguish the two possible types, equation (4.14) gives

$$c_{\mathrm{g}}^{-} = c_{\mathrm{g}}^{+} = V(h_*) + h_* V'(h_*), \quad = Q'(\rho_*), \tag{6.2}$$

at onset, where $\rho_* = 1/h^*$, and

$$Q(\rho) = \rho \hat{V}(\rho), \tag{6.3}$$

with $\hat{V}(\rho) = V(1/\rho)$. Relation (6.3) is the so-called *fundamental diagram* relating macroscopic flow and density. Equation (6.2) then captures the well-known property of hydrodynamic theory that the local wave-propagation speed is equal to the gradient of the fundamental diagram.

To guarantee that the onset of instability is convective *upstream*, it thus suffices to parametrise one's car-following model so that the first instability (as sensitivity is reduced) occurs to the right of the fundamental diagram's maximum value, so that $Q'(\rho^*) < 0$.

Finally, note that the locus of $c_g^- = 0$ corresponds in general to the maximum of the fundamental diagram at which $Q'(\rho^*) = 0$ — a condition which is independent of the sensitivity (α or a), thus giving rise to the vertical sections of dashed line in figures 8(a,b).

7. Conclusion

The message of this paper is that there are important distinctions in the type of instability that highway traffic models display. The concepts presented here are standard in the Mathematical wave propagation literature (Huerre & Rossi, 1998, Sec. 3), but are not appreciated by traffic modellers and in particular the microsimulation community. However, we view the stability properties as an essential part of the design and parametrisation of car-following models. Firstly, no good simulation model should display *platoon instability*, see equation (3.5). Secondly, if a model displays *string instability*, then one should consider how it propagates disturbances relative to the frame of the road. Our view is that only convective upstream (type C_u) instability should be allowed. This is because spatio-temporal patterns in detector data which display growth only do so in the upstream direction. However, we should emphasise that the absence of downstream growth in data does not rule out downstream linear instability (of types C_d and A), if it is combined with more complicated model features (e.g., nonlinearity, or spatial heterogeneity at junctions). Thus the arguments presented here should be viewed only as the first step in a more detailed modelling debate.

We have seen that there are two quantities which can be used to describe the overall wave propagation properties and classify the direction of instability. These are the *group velocity* (§4) and the *signal velocity* (§5). The group velocity describes the propagation of wave packets, whereas the signal velocity describes how a new disturbance penetrates a medium which is initially at rest. Our view is that traffic instability is triggered by instantaneous microscale events in the vicinity of junctions, and so the signal velocity is the correct measure to determine the envelope of the resulting disturbance and so classify the type of instability.

Unfortunately, the calculation of the signal velocity is more complicated than that for the group velocity, but in principle all of the steps shown here can be automated using automatic differentiation and root-finding methods, if a car-following model were to be supplied as a black-box routine which complies with the structure described in §2. However, more work is required to generalise the model structure still further, for example, to incorporate reaction-time delay and multi-anticipation effects.

Finally, an example of the kind of practical lesson that can be achieved by our analysis is displayed in figure 8 — which although it is model-specific, suggests more broadly that the undesirable types of string instability (convective downstream C_d and absolute A) may be eliminated if models are parametrised so that linear instability is only marginal. Recent analysis of empirical stop-and-go wave data (Zielke *et al.*, 2008) has indicated surprisingly small growth rates which are consistent with

the suggestion that linear instability is a marginal effect. However, an alternative perspective (Wilson, 2008) for further investigation is that nonlinear stability properties are also crucial in determining the overall wave propagation properties.

We thank Martin Treiber who brought this problem area to our attention at a meeting in Hamburg in October 2007, and for interesting conversations with him since, in Vienna (May 2008) and in Dresden (April 2009). JAW acknowledges the support of the Science Foundation Ireland (grant ref. 06/MI/005). REW acknowledges the support of EPSRC Advanced Research Fellowship EP/E055567/1 and the Highways Agency for access to MIDAS inductance loop data.

References

Bando, M., Hasebe, K., Nakayama, A., Shibata, A. & Sugiyama, Y. (1995), 'Dynamical model of traffic congestion and numerical simulation', *Phys. Rev. E* **51**(2), 1035–1042.

Bender, C. M. & Orszag, S. A. (1999), *Advanced Mathematical Methods for Scientists and Engineers*, Springer-Verlag.

Brackstone, M. & McDonald, M. (1999), 'Car-following: a historical review', *Transportation Research Part F* **2**(4), 181–196.

Brillouin, L. (1960), *Wave Propagation and Group Velocity*, Academic Press Inc. (London) Ltd.

Chandler, R., Herman, R. & Montroll, E. (1958), 'Traffic dynamics: Studies in car following', *Operations Research* **6**(2), 165–184.

Garrett, C. & McCumber, D. (1970), 'Propagation of a Gaussian light pulse through an anomalous dispersion medium', *Phys. Rev. A* **1**(2), 305–313.

Helbing, D. (2001), 'Traffic and related self-driven many-particle systems', *Rev. Mod. Phys.* **73**(4), 1067–1141.

Helbing, D. & Johansson, A. F. (2009), 'On the controversy around Daganzo's requiem for and Aw-Rascle's resurrection of second-order traffic flow models', *The European Physical Journal B* **69**, 549–562.

Helbing, D., Treiber, M., Kesting, A. & Schönhof, M. (2009), 'Theoretical vs. empirical classification and prediction of congested traffic states', *The European Physical Journal B* **69**, 583–598.

Herman, R., Montroll, E. W., Potts, R. B. & Rothery, R. W. (1959), 'Traffic dynamics: Analysis of stability in car following', *Operations Research* **7**(1), 86–106.

Huerre, P. & Rossi, M. (1998), Hydrodynamic instabilities in open flows. In *Hydrodynamics and Nonlinear Instabilities* (eds C. Godreche & P. Manneville), pp. 91–294.

Jiang, R., Wu, Q. & Zhu, Z. (2001), 'Full velocity difference model for a car-following theory', *Phys. Rev. E* **64**, 1–4.

Kerner, B. S. & Rehborn, H. (1996), 'Experimental properties of complexity in traffic flow', *Phys. Rev. E* **53**, 4274–4278.

Kerner, B. S. & Rehborn, H. (1997), 'Experimental properties of phase transitions in traffic flow', *Physical Review Letters* **79**(20), 4030–4033.

Kerner, B. S. (2002*a*), 'Empirical macroscopic features of spatial-temporal traffic patterns at highway bottlenecks', *Phys. Rev. E* **65**, 1–30. Art. No. 046138.

Kerner, B. S. (2002*b*), 'Synchronized flow as a new traffic phase and related problems for traffic flow modelling', *Mathematical and Computer Modelling* **35**, 481–508.

Kesting, A. & Treiber, M. (2008), 'How reaction time, update time, and adaptation time influence the stability of traffic flow', *Computer-Aided Civil and Infrastructure Engineering* **23**, 125–137.

Mitarai, N. & Nakanishi, H. (2000), 'Convective instability and structure formation in traffic flow', *Journal of the Physical Society of Japan* **69**, 3752–3761.

Schönhof, M. & Helbing, D. (2009), 'Criticism of three-phase traffic theory', *Transportation Research Part B* **43**, 784–797.

Treiber, M., Hennecke, A. & Helbing, D. (2000), 'Congested traffic states in empirical observations and microscopic simulations', *Phys. Rev. E* **62**(2), 1805–1824.

Treiber, M., Kesting, A. & Helbing, D. (2010), 'Three-phase traffic theory and two-phase models with a fundamental diagram in the light of empirical stylized facts', *Transportation Research Part B* **44**, 983–1000.

Wang, L., Kuzmich, A. & Dogariu, A. (2000), 'Gain-assisted superluminal light propagation', *Nature* **406**(6793), 277–279.

Ward, J. A. (2008), Heterogeneity, Stability and Lane-Changing in Traffic, PhD thesis, University of Bristol, UK.

Wilson, R. E. (2008), 'Mechanisms for spatiotemporal pattern formation in highway traffic models', *Philos. Transact. A Math. Phys. Eng. Sci.* **366**, 2017–2032.

Wilson, R. E & Ward, J. A. (2010), 'Car-following models: Fifty years of stability analysis—a mathematical perspective', *Transportation Planning & Technology* **34**(1), 3–18.

Zielke, B. A., Bertini, R. L. & Treiber, M. (2008), 'Empirical measurement of freeway oscillation characteristics', *Transportation Research Record* **2088**, 57–67.

Appendix A. Details of the small wavenumber expansion

In §4, we introduced the perturbation expansion for λ_+ in terms of the real coefficients $\lambda_1, \lambda_2, \ldots$, which we solved for up to second order. Furthermore, we showed that $\lambda_1 < 0$ and the sign of λ_2 controls stability. In this section we prove that $\lambda_3 > 0$ and $\lambda_4 < 0$ when $\lambda_2 > 0$, i.e. when the system is unstable.

Collecting the third order terms in the small θ perturbation expansion of the dispersion relation given by equation (4.2), we find

$$\lambda_3 = \frac{1}{6f_v}\left(6\lambda_2\left[f_{\dot{h}} + 2\lambda_1\right] + 3f_{\dot{h}}\lambda_1 - f_h\right). \tag{A 1}$$

Using equation (3.3) we observe that

$$\left[f_{\dot{h}} + 2\lambda_1\right] = \frac{1}{f_v}\left[f_{\dot{h}}f_v + 2f_h\right] < 0 \quad \text{when} \quad \lambda_2 > 0, \tag{A 2}$$

since

$$0 < \frac{f_v^2}{2} + f_h < f_{\dot{h}}f_v + 2f_h. \tag{A 3}$$

Thus when $\lambda_2 > 0$, all the grouped terms in parenthesis in equation (A 1) have negative sign and therefore $\lambda_3 > 0$. Collecting the fourth order terms, we find

$$\lambda_4 = \frac{1}{24f_v}\left(24\lambda_2^2 + f_{\dot{h}}\lambda_2 - 24\lambda_3\left[f_{\dot{h}} + \lambda_1\right] - 4\lambda_1\left[6\lambda_3 - f_{\dot{h}} + \frac{f_v}{4}\right]\right). \tag{A 4}$$

Using the same argument as before, when $\lambda_2 > 0$, we find

$$-24\lambda_3\left[f_{\dot{h}} + \lambda_1\right] > 0, \tag{A 5}$$

and

$$\begin{aligned} &-4\lambda_1\left[6\lambda_3 - f_{\dot{h}} + \frac{f_v}{4}\right] = \\ &-\frac{4\lambda_1}{f_v}\left[6\lambda_2\left(f_{\dot{h}} + 2\lambda_1\right) + 3f_{\dot{h}}\lambda_1 + \left\{\frac{(f_v)^2}{2} - f_{\dot{h}}f_v - f_h\right\} - \frac{(f_v)^2}{4}\right] > 0, \end{aligned} \tag{A 6}$$

since all the grouped terms in square brackets are negative. Thus when $\lambda_2 > 0$, all the grouped terms in parenthesis in equation (A 4) have positive sign and therefore $\lambda_4 < 0$.

Appendix B. Details of the saddle selection procedure

We now give further details of the selection of the saddle point z_* required in the signal velocity calculation as described in §5. This is a rather technical argument which the end-user may skip. Recall that we seek saddle points of $\rho(z)$ defined by equation (5.8), which are thus roots of the cubic equation (5.11) parametrised by f_h, $f_{\dot{h}}$, f_v and κ. Ultimately we are interested in calculating the correct choice of saddle as κ is varied. However, here we develop the prescription for fixed (but general) values of all of the parameters including κ.

Because the cubic equation (5.11) has real coefficients, $\rho(z)$ has generically either three real saddles or a single real saddle and a complex conjugate pair. Our tactic is to analyse the local behaviour of $\rho(z)$ at the real saddle(s) and to determine whether the direction of their curvature is suitable for employment in the steepest-descent method. If no real saddle can be used, we infer that the complex conjugates must be chosen instead.

When a candidate saddle has thus been identified, the global geometry must be checked to ensure that the original contour $\mathcal{C} = (\gamma - \mathrm{i}\infty, \gamma + \mathrm{i}\infty)$ can be deformed to pass through the saddle without crossing singularities. Moreover, we require that $\phi(z) := \mathrm{Re}(\rho(z))$ attains not only a local maximum but also its *global* maximum on the deformed contour $\mathcal{C}'$ at the selected saddle point. In practice this last point can be checked by inspecting the level set geometry of $\phi(z)$ and ensuring that $\mathcal{C}'$ does not re-cross the level sets which emanate from the saddle.

We shall seek deformed contours $\mathcal{C}'$ which are symmetric about the real axis in the complex plane, and which thus cross the real axis orthogonally, i.e., parallel to the imaginary axis at the point of crossing. If ϕ has a local maximum in the imaginary direction at real z_*, then by the Cauchy-Riemann equations, ϕ has a local minimum in the real direction. Real saddles of ϕ thus correspond to turning points of the real function

$$\phi(x) = x + \kappa \log \left| \frac{p(x)}{q(x)} \right|, \tag{B 1}$$

and candidates for the steepest-descent method correspond to local minima. Here x is real, and we define

$$p(x) := f_{\dot{h}} x + f_h, \tag{B 2}$$

and

$$q(x) := x^2 + (f_{\dot{h}} - f_v)x + f_h. \tag{B 3}$$

The key simplification is that we may analyse the real geometry of equation (B 1) without solving the cubic equation (5.11), but rather by studying its (real) singularities, which are of two types:

- P: the single zero $-f_h/f_{\dot{h}}$ of $p(x)$. Note $\phi(x) \to -\infty$ as $x \to \mathrm{P}\pm$.
- Q: the real zeroes of $q(x)$, if there are any. These correspond to the platoon eigenvalues that solve equation (3.5). Note $\phi(x) \to +\infty$ as $x \to Q\pm$.

Note also that $\phi(x) \to -\infty$ as $x \to -\infty$ and $\phi(x) \to +\infty$ as $x \to +\infty$. The geometry of $\phi(x)$ may thus be classified according to the order of the singularities on the real line, which we may describe intuitively via the notation QQP, QPQ, PQQ, or P. Here case P denotes when the platoon eigenvalues are complex.

We now analyse how the singularity structure depends on the choice of parameters f_h, $f_{\dot{h}}$, f_v and κ. To simplify the study, we observe that a non-dimensional time $\hat{t} = t\sqrt{f_h}$ can be introduced, for example in equation (3.4). This eliminates the parameter f_h and introduces re-scaled parameters $\tilde{f}_{\dot{h}} := f_{\dot{h}}/\sqrt{f_h}$ and $\tilde{f}_v := f_v/\sqrt{f_h}$ and subsequently $\tilde{\kappa} := \kappa/\sqrt{f_h}$. Hence in what follows, we set $f_h = 1$ and analyse how the problem depends on $f_{\dot{h}}$, f_v and κ only, where the 'tildes' are dropped for notational convenience.

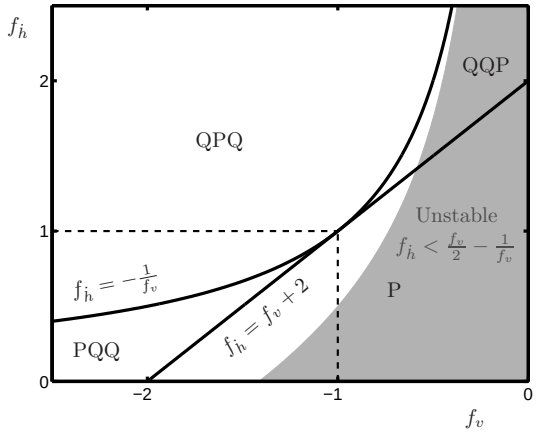

Figure 9. Illustration of the $(f_v, f_{\dot{h}})$ plane which is split into four regions according to the order of the singularities of $\phi(x)$, namely QQP, QPQ, PQQ and P. These regions are bounded by the curves $f_{\dot{h}} = f_v + 2$ (double root of $q(x)$) and $f_{\dot{h}} = -1/f_v$ (at which one of the roots of $q(x)$ coincides with the root of $p(x)$). The region of instability is shaded in grey. Note that only the QQP and P regions occur for parameters corresponding to instability.

The order of the singularities of $\phi(x)$ is independent of κ, and so may be described entirely in terms of the $(f_v, f_{\dot{h}})$ parameter plane. See figure 9. Here the boundaries between the different classes can be described analytically, and in particular, it may be proven that only cases QQP and P occur for parameters corresponding to instability. For these cases, the putative geometries for ϕ and a notation to describe them are shown in figure 10.

The next task is to investigate which of the geometries in figure 10 are actually achieved, as κ is varied. This is a problem with intriguing mathematical structure, but to simplify matters, we have addressed it by numerical search. The results are summarised in figure 11. In each of the sub-plots, κ is held fixed, and the geometry in the $(f_v, f_{\dot{h}})$ plane is analysed. To focus attention on parameters corresponding to instability, the horizontal axis in these pictures is re-scaled so that the unstable regime is a rectangular strip which fills the scope of each sub-plot.

We find

- The QQP cases (0,1,0,0) and (0,1,0,2) and the P cases (1,0) and (1,2) dominate for most parameters. For these, the simple saddle selection rules as presented in §5 apply.

- There is a thin slice of parameters confined to $0 < \kappa < 0.1$ (or $0 < \kappa < 0.1\sqrt{f_h}$ in the dimensional units used in the main body of the paper) where cases (0,1,2,0) and (3,0) occur. For these, the middle saddle should actually be selected. To clarify: if the real saddles are given by $z_1 < z_2 < z_3$, then z_2 should be selected. These rare cases are contrary to the usual prescription given in §5.

- The cases (0,3,0,0) and (2,1,0,0), which have no admissible saddles, do not occur. In fact, this result can be proved rigorously by considering the small

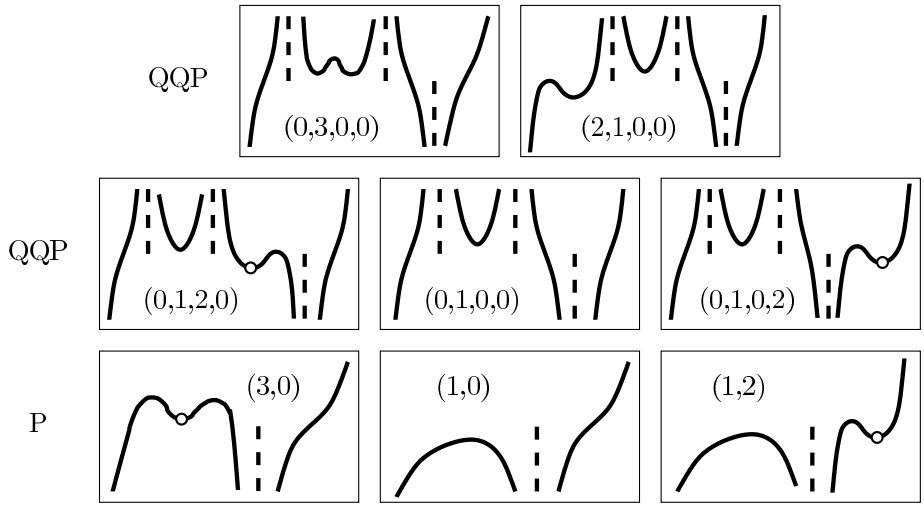

Figure 10. Putative geometries for $\phi(x)$ for the cases QQP and P. Singularities are marked with dashed lines. Each distinct case is labelled according to the number of saddle points and their position relative to the singularities. For example, case (1,2) (bottom right) has a singularity P with one saddle to the left and two to the right. Saddle points that lie on the real line and satisfy the selection criteria are indicated by circular markers. Cases (1,0) and (0,1,0,0) have admissible complex conjugate saddles. In contrast, cases (0,3,0,0) and (2,1,0,0) have no admissible saddles, because there are no local minima to the right of both Q singularities. Consequently, the contour deformation would involve crossing the poles of $\phi(z)$. However in figure 11 we show that cases (0,3,0,0) and (2,1,0,0) do not occur in practice.

and large κ limits of the cubic equation (5.11) and its derivative with respect to κ, however this analysis is beyond the present discussion.

Finally, figure 12 shows the level set geometry of $\phi(z)$ and the saddle selection procedure and deformed contours for each of the six geometries that occur. These plots establish that the rules described above provide saddles and contours which satisfy the global geometric constraints of the steepest-descent method.

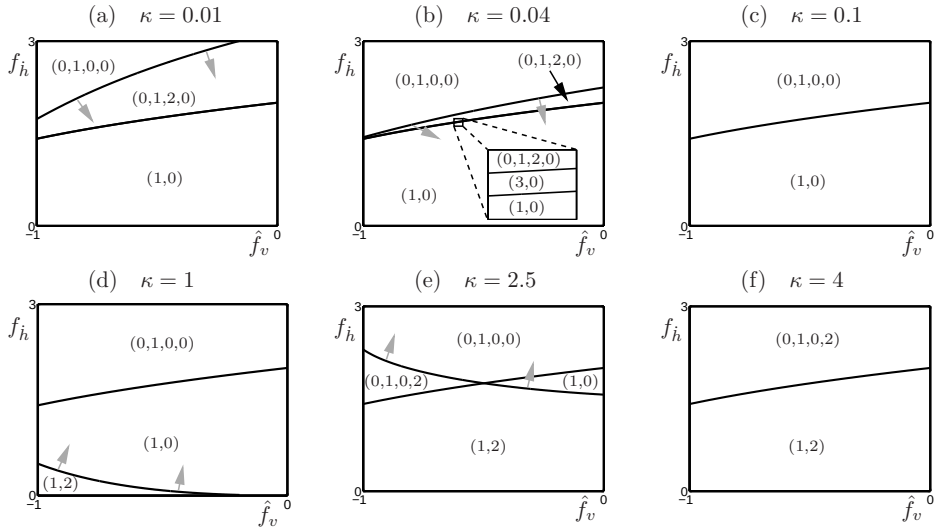

Figure 11. Rescaled $(\hat{f}_v, f_{\dot{h}})$ plane where $\hat{f}_v = -f_v/(f_{\dot{h}} - \sqrt{(f_{\dot{h}}^2 + 2)})$, i.e. the stability boundary is given by $\hat{f}_v = -1$. Panels (a)–(f) illustrate where the possible geometries of $\phi(x)$ occur as κ is increased. Each region is labelled according to the notation introduced in figure 10 and the motion of the boundaries as κ increases is indicated by the grey arrows. The inset in panel (b) is a zoom of the tiny region around the QQP/P boundary where geometry of type (3,0) occurs.

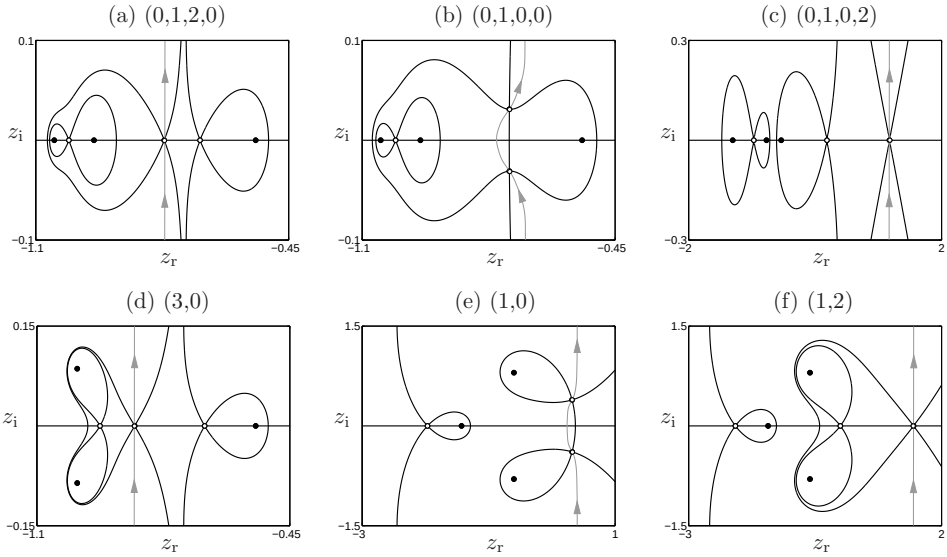

Figure 12. Contour plots of $\phi(z)$ for each of the cases introduced in figure 10. The grey lines indicate the deformed integration contour $\mathcal{C}'$. Singularities are indicated by black markers and saddle points by white markers.